Characterization of thermoelectric generator modules: Numerical and analytical study on heat flow determination under transient temperature conditions

Jhonatan Samuel Ferrer Caro ✉ ⑩ ; Eckhard Müller ⑩ ; Pawel Ziolkowski ⑩

Check for updates

View Online

Export Citation

09 December 2024 11:36:47

Characterization of thermoelectric generator modules: Numerical and analytical study on heat flow determination under transient temperature conditions

View Online   Export Citation   CrossMark

Jhonatan Samuel Ferrer Caro,[1,a] (iD) **Eckhard Müller,**[1,2] (iD) **and Pawel Ziolkowski**[1] (iD)

AFFILIATIONS

[1] German Aerospace Center (DLR) – Institute of Materials Research, Linder Höhe, D-51147 Cologne, Germany

[2] Institute of Inorganic and Analytical Chemistry, Justus Liebig University Gießen, Heinrich-Buff-Ring 17, D-35392 Gießen, Germany

[a] Author to whom correspondence should be addressed: jhonatan.ferrer@dlr.de

ABSTRACT

Thermoelectric generator modules (TEMs) are in common use as power sources for spacecraft. Here, we present the first investigations on a modified characterization approach for TEM with a focus on the heat flow determination under transient temperature boundary conditions with a reference block as a heat flow meter. Furthermore, we present a solution of a partial differential equation (PDE) for determining temperature fields under transient boundary conditions in single thermoelectric blocks. The PDE solution serves likewise as a reference for a numerical model using OpenModelica with a network model of the TEM measurement facility under ideal measurement conditions without parasitic heat losses. Heat flow results obtained from the numerical model are compared with the simulated transient measurement procedure, which has been derived from an analytic description of the heat conduction in the measurement configuration.

INTRODUCTION

Thermoelectric modules (TEMs), which build the base for the construction of thermoelectric generators (TEGs), convert heat directly into electricity due to the Seebeck effect. Accordingly, a TEM consists of a multitude of n- and p-type thermoelectric (TE) legs, which are connected by metallic bridges to form thermocouples capable of generating a thermovoltage in response to a temperature difference across the legs. The efficiency of TE energy conversion equals the ratio of the electrical power output, P, of the TEM to the incident heat into the hot side of the TEM, $\dot{Q}_{\text{in}}^{\text{TEM}}$,[1]

$$\eta = \frac{P}{\dot{Q}_{\text{in}}^{\text{TEM}}}. \qquad (1)$$

Based on the constant properties model (CPM), i.e., assuming TE properties being independent of temperature, the maximum efficiency of the TEM, η_{max} is described as[2]

$$\eta_{\text{max}} = \frac{T_h - T_c}{T_h} \cdot \frac{\sqrt{1 + ZT_{\text{m}}} - 1}{\sqrt{1 + ZT_{\text{m}}} + \frac{T_c}{T_h}}, \qquad (2)$$

and is limited by the Carnot efficiency

$$\eta_c = \frac{T_h - T_c}{T_h}, \qquad (3)$$

which is related to the temperatures at the hot side T_h and cold side T_c of the TEM. Furthermore, the physical properties and the loss mechanisms of the thermoelectric materials and the TEM device affect the η_{max} by the thermoelectric figure of merit ZT_{m}, which is defined according to the following equation:

$$ZT_{\text{m}} = \frac{S^2 T_{\text{m}}}{R \cdot K}, \qquad (4)$$

where S is the effective Seebeck coefficient of the module, which is ideally, neglecting any inner parasitic temperature drop inside the TEM, $S = N \cdot (S_p - S_n)$, with N being the number of thermocouples in the TEM, and S_p, S_n being the Seebeck coefficient of the p-type legs and n-type legs, respectively. In Eq. (4), $T_m = (T_h + T_c)/2$ is the mean temperature of the module, R is the electrical resistance of the TEM, and K is the thermal conductance.[3] During the last decades, much effort has been invested in improving the performance of TE materials, which has resulted in ZT values between 1.1 and 2.2.[2–5] In turn, this has led to TEM efficiencies of up to 12%.[6–8] Still, the existing limitations on the accuracy and repeatability of employed TEM characterization techniques raises questions about the incremental improvement of TEG efficiencies over the past years since some of the reported improvement could be due to uncertainty related to applied measurement methods.

Characterization techniques can be divided into steady state and transient methods. These can be further split into those that determine η, based on measurements of electrical power output P and incident heat flow, $\dot{Q}_{in}^{TEM}$ [Eq. (1)] or from a calculation using a measured value of ZT_m [Eq. (2)]. The former are usually implemented as steady state methods, and the latter by the Harman[9] and impedance spectroscopy methods,[10] which are referred to as transient methods. Alternatively, steady state characterization with direct measurement of the power output and incident heat is more common due to the high temperature differences applied, which are also found in the typical operation environments of TEM. Likewise, the calculation of η from ZT_m measured under large temperature differences is also possible.[11] However, the CPM as the theoretical fundament of Eq. (2) neglects relevant effects on the TEM performance such as Thomson heat and the asymmetric distribution of Joule heat along the TE legs.[12]

Among the steady state characterization methods, the widest-spread technique is the reference principle.[13–15] Although measurement procedures and instrumentation have been reported, such as by König et al.[16] and Man et al.,[17] underlying sources of uncertainty are often unknown for many measurement devices due to the low level of their standardization, which are manifested through the absence of measurement guidelines and reference samples for TEG metrology.[18–24] Other works published uncertainty analyses of the Seebeck coefficient and electric resistivity[25–27] as well as for zT characterization.[28] However, a recent introduction of measurement guidelines for TEM characterization seeks to reduce uncertainty sources.[29,30] Currently, the TEM efficiency is deduced from heat flow data, which are measured by reference or absolute characterization techniques in a custom-made TEG measurement apparatus (TEGMA).[31] The reference method employs at least one heat flow meter (HFM), which is placed thermally in a serial connection with the TEM under test and is equipped with thermocouples for the determination of the heat flow (Fig. 2). The heat flow is determined from the temperature gradient inside the HFM, which is measured by at least two thermocouples in drillings placed along the center line of the HFM. Since the reference method can involve a hot side HFM (HSHFM) and a cold side HFM (CSHFM), the HFM and location therein of the thermocouples are noted by superscripts h or c and numbering subscript i, respectively. The distance between neighboring thermocouples, $\Delta z_i = z_{i+1} - z_i$, can vary. The thermocouple sensors give access to the temperature differences, $\Delta T_i = T_{i+1}^h - T_i^h$,

$$\dot{Q}_{in}^{TEM} = \kappa_{HFM} A_{HFM} \frac{\Delta T_i}{\Delta z_i}, \quad i = 0, 1, 2, 3, \ldots. \tag{5}$$

Equation (5) is linked to the incident heat flow $\dot{Q}_{in}^{TEM}$ at the hot side of the TEM but can be employed analogously for a determination of the outgoing heat flow at the cold side of the TEM, $\dot{Q}_{out}^{TEM}$, if an HFM is installed there. In Eq. (5), the distance between thermocouples, Δz_i, the thermal conductivity of the HFM material, κ_{HFM}, and the cross-section area of the HFM, A_{HFM}, are involved. Furthermore, Eq. (5) implies a constant properties model (CPM) for κ_{HFM}, which is specified as an averaged value within the operating temperature interval of the HFM.[32] Equation (5) can be expanded to local measurements of temperature gradients using neighboring or more than two thermocouples. Pairs of neighboring thermocouples define segments, in which the Fourier heat flow is determined for every segment of the HFM. The incident (or outgoing) heat flow of the TEM can be expressed in a steady-state measurement as a mean heat flow value from all evaluated segments.

$\dot{Q}_{out}^{TEM}$ describes the Fourier heat flow into the cold side HFM (CSHFM). Thermocouple signals are likewise used to trace the thermal stability of the measuring section and to control the temperature conditions by installed temperature controllers, which adjust the released and absorbed heat of installed heaters and cooling plates. Thermal stability is detected by evaluation of the residual drift of temperature data from sensors installed in the components of the measuring section, i.e., from permanent components such as a heater and cooling plate, heat exchangers, and HFM adapted to the cross section of the TEM under test. However, due to the required temperature stabilization period after each change of the sample temperature and, due to Peltier heat transport, also after varying the electric current through the TEM, the full module characterization may last up to one to two weeks[31] with a reasonable number of temperature setpoints and values for electric current flow.

Alternatively, a method of accelerating the characterization is given by conducting measurements under transient temperature conditions without thermal stabilization but under a continuous temperature drift of the sample. For this approach, additional effects on the TEM sample and HFM must be considered, which are represented by the heat capacity of the involved components.

Local heat flow and heat absorbed along an individual segment in Fig. 1 can be defined as $\dot{Q}_F$ and $\dot{U}$, respectively. Therefore, assuming ever smaller segment length $\Delta z_i \to dz$ and time increment $\Delta t \to dt$ means that $\dot{Q}_F \to \kappa_{HFM} A_{HFM}\, dT/dz$ and $\dot{U} \to \Delta m_{HFM} c_{HFM} dT/dt$, respectively,[33] where $\Delta m_{HFM} = \rho_{HFM} A_{HFM} dz$. An approximation of the heat flow balance at a segment inside a HFM block at a specific time is obtained as

$$\dot{Q}(z_{i+1}, t) = \dot{Q}(z_i, t) - \dot{U}_i(t). \tag{6}$$

This equation tells us that the heat flow in a transient process is different in any individual segment of a HFM, which is due to the involved heat capacities, C_{HFM}. Consequently, a transient characterization method must allow for measurement of both the spatial temperature profile at a given time as well as the time-dependent temperature evolution.
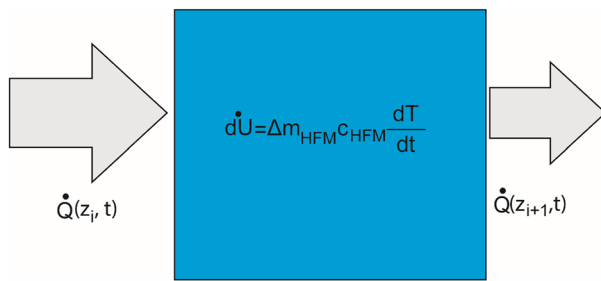
09 December 2024 11:36:47

FIG. 1. Local segment in a HFM with transient temperature boundary conditions (BC) where the left side temperature is higher than the right side temperature. The incoming heat flow, $\dot{Q}(z_i, t)$ [Eq. (6)] into the segment at (z_i, t), is equal to the increment amount of energy stored in the segment, $\dot{U}$, per time interval, dt, used to raise the temperature of the segment plus the heat $\dot{Q}(z_{i+1}, t)$, leaving the segment. The mass of the segment, Δm_{HFM}, is dependent on the density of the HFM, ρ_{HFM}, and is integrated over the length Δz_i of the segment. The specific heat of the HFM material c_{HFM} gives finally access to the heat capacity of the segment $C_{HFM} = \Delta m_{HFM} \cdot c_{HFM}$.

Therefore, here we report on the development of a measurement procedure for the determination of heat flow under transient temperature conditions, which we will call here "transient measurement function" (TMF), which is the definition of a procedure to be executed by the TEGMA facility. Before its implementation in the hardware of the facility, the TMF is merely implemented virtually here, as a digital twin, extracting simulated temperature measurement values from a transient OpenModelica (OM) simulation of a TEM measurement setup. The TMF assumes ideal measurement conditions only, effectively neglecting the impact of thermal transfer resistances at component interfaces or parasitic heat losses. The TMF is derived from the analytical solution of the time dependent heat flow equation for the specific conditions of the employed heat flow meter in a reference principle measurement setup. The virtual TMF implementation uses temperature data from the CSHFM in the OM digital twin as simulated measurement input to evaluate the segment-wise absorbed heat and Fourier heat. Practically, the TMF is compiled in OM. To test the accuracy and applicability of the TMF, a corresponding network model of the measurement set-up is presented here, which assumes one-dimensional (1D) heat flow through components of the measuring section, including heaters, HFMs, TEM samples, and a cooling plate for heat extraction. The network model was implemented with the OM software.[34]

With regard to how the transient effects affect the temperature profile at the TEM, Fig. 2(b) vs Fig. 2(c) highlight this difference, where Fig. 2(b) displays the steady state and Fig. 2(c) the transient case.

In Fig. 2, the essential difference in the temperature profiles between the stationary (b) and transient (c) cases consists in the change of the inner energy of the material $\dot{U}$, which is locally absorbed when the temperature of the HFM is steadily raised. This bows the temperature profile along the HFM down. Vice versa, during cooling mode, $\dot{U}$ is released, bowing the temperature profile upward.

The challenge arises on how we can conclude on steady state TEM characteristics of interest, such as maximum electric power output and maximum conversion efficiency, from measurement results obtained under transient temperature boundary conditions. Usually, TEM modules are used under steady state operating conditions (see, e.g., Champier,[35] Jouhara et al.[36]); hence, the common characteristics of interest are steady state measurands. This might render unusable the measurands determined under transient conditions to speed up characterization, as far as the measurands will be overlaid by transient effects. To separate and eliminate transient effects from the evaluation of a transient measurement, analyzing the partial differential equation (PDE) that governs the temperature profile of an HFM or TE leg is straight-forward. We will see that the PDE can be split into steady-state and transient contributions, which will provide access to steady state measurands in a transient measurement process. Earlier works have applied transient analysis to conclude on measurands, starting with Harman et al.,[37] who introduced a method to measure zT when switching a DC electric current flow. Derivates of this method were further developed, including the so-called "transient method," which will be referred to in this paper as the current-induced method, where the thermovoltage or Seebeck-caused component and the resistive component of voltages were measured with high sampling rate and bandwidth electronics as explained by Rowe et al.[38] Other works with this method have been provided by Kwon et al.,[39] who showed that parasitic losses affected zT measurements by up to 28%. Due to such parasitic effects, Ao et al.,[40] Kang et al.,[41] and Roh et al.[42] have worked on corrective procedures. Another method first introduced by De Marchi et al.[43] is the porcupine method based on impedance spectroscopy. In this method, an AC frequency sweep is supplied to the TEM. The frequency response of the TEM is tapped by measuring real and imaginary signal contributions of the TEM voltage. The TEM efficiency is derived from an evaluation of characteristic parameters of this frequency response. Nevertheless, all of these methods drive thermal transients by an internal electrical excitation of the TEM, which typically allows for a maximum variation of temperature differences across the TEM of a few and up to some tens of Kelvin only due to the limited contribution of the Peltier heat flow to the overall heat balance of a TEM. The transient method suggested in this work applies transient thermal conditions at the TEM from the outside by controlling temperatures of heaters and cooling plates. This effectively allows for an application-relevant TEM characterization under continuously drifting temperature differences up to hundreds of Kelvin, while simultaneously saving time compared to steady-state approaches since measurements are conducted concurrently without requiring any stabilization period. However, measurements under transient temperature conditions require instead a short initial waiting time since the temperature functions are influenced by transient signal contributions when a temperature drift is started. As will be shown later, derivation of measurands representative for steady-state conditions becomes accessible after an initial waiting time for the relaxation of fully transient contributions, which have to be excluded from data evaluation, effectively limiting the reported transient measurement approach to a quasi-stationary time domain of TEM measurements. The measuring instrumentation and sample installation of this method are similar to the wide-spread steady state reference method and shall
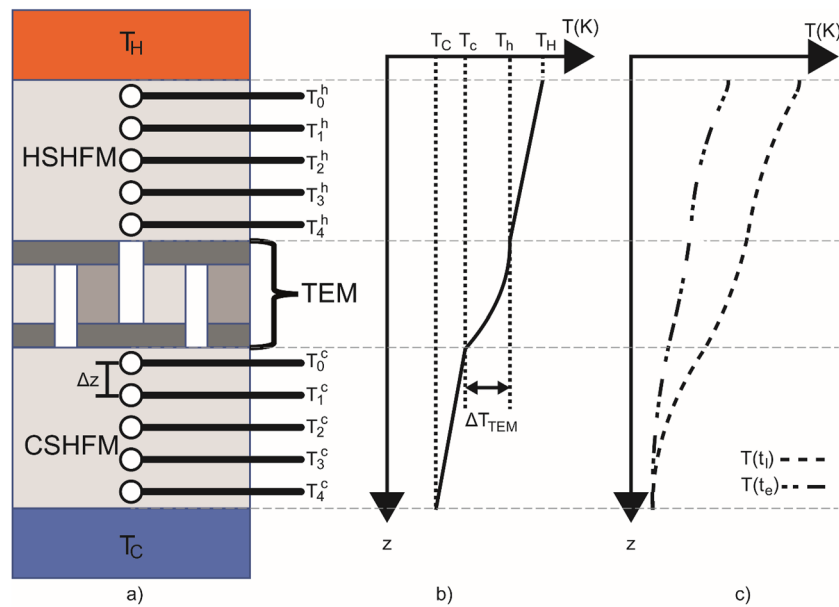
FIG. 2. Schematic of the reference method for heat flow determination (a) with thermocouple locations along the z axis of two HFM, a TEM sample, and a heat source and heat sink located at the top and bottom, respectively. (b) Qualitative temperature profile along the column for thermal steady state operation under electric current flow through the TEM; (c) transient temperature evolution along the column at an early simulation time, t_e, and at a later time, t_l. In this example, the transient temperature evolution along the column is the result of a steady temperature increase in the heater, while the sink temperature is kept constant. Additionally, for a current flow throughout the TEM, the axial temperature profile inside the TEM bows up for both (b) due to a parabolic contribution of Joule heat to the temperature profile along the TE legs, and to a lesser extent for (c) due to an additional contribution of the heat capacity, which is in the case of the depicted heating sequence of the column represented in temperature profiles by a rational function with a negative magnitude due to the occurring heat absorption of involved components. The heat capacity contribution also causes a corresponding bow of the temperature profiles in the HSHFM and CSHFM sections of (c).

likewise provide a full TEM characterization including heat flow, power output, efficiency, and further essential TEM properties like the internal electrical resistance, optimum current for maximum power or maximum efficiency, respectively, and the integral Seebeck coefficient and thermal resistance. The current work presents a development for such a transient TEM characterization with a focus on the analytical basics of the evolution of the 1D transient temperature profile and a procedure for measurement of heat flow.

The 1D PDE of the local energy balance for a block of material that may represent a HFM without thermoelectric effects (passive block) or a resistive material under DC in transient operating conditions is derived and validated against a virtual copy of the block in an OM model. From this PDE, one temperature evolution equation with two temperature domains, a transient and a quasi-stationary, is found. Furthermore, from the transient equation, the relaxation time of the block to only quasi-stationary conditions after applying a perturbation can be obtained. The PDE solution for a single block under transient temperature conditions builds the base for referencing to the numerical simulation, which is used to test the applicability of the TMF in the simulation of a complete measurement environment. A virtual representation of the TMF is tested with an OM model of a homogeneous material block.

METHODS

Method 1: Analytical solution of the transient temperature profile in a material block assuming CPM

In thermal steady-state operation without heat loss by radiation and convection [Fig. 2(b)], the temperature difference between the heater, T_H, and cooler, T_C, is maintained constant and piecewise linear temperature profiles can be expected along every component of the measuring assembly in a 1D heat flow situation. Neglecting parasitic heat loss and assuming the electrical open loop condition of the TEM (zero electric current flow), the Fourier heat is constant along the entire column. The gradient of the temperature profile in each segment is inversely proportional to the local thermal conductivity. Temperature steps along the temperature profile at interfaces stem from the thermal contact resistance. Under thermal steady-state conditions, the involved heat capacities do not affect the temperature profile, $\dot{U} = 0$,[33] since there is no temperature change over time. Consequently, only Fourier heat, $\dot{Q}_F$, is crossing the HFM and TEM.

On the contrary, operating a TEM in the energy conversion mode (e.g., current flow ≠ 0), the incident and released heat at the hot and cold sides of the TEM, respectively, differ from each other by the exported electrical power due to the principle of
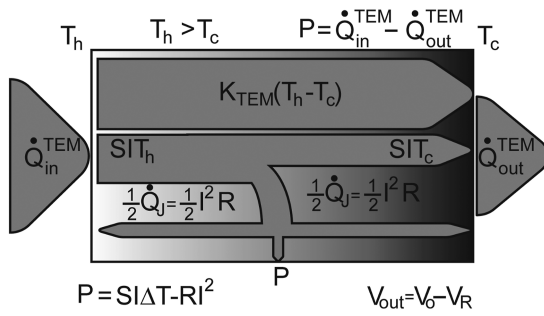
FIG. 3. Schematic of the energy flow in a TEM (CPM case) in stationary energy conversion mode.[32] The exported electrical power P is equivalent to the difference between the incident heat flow $\dot{Q}_{in}^{TEM}$ and the ejected heat flow $\dot{Q}_{out}^{TEM}$ at the cold side of the TEM. The electrical power generated depends on the temperature difference across the TEM, its Seebeck coefficient, and its internal electric resistance.

conservation of energy. By conduction of an electric current through the TEM, Peltier heat will be absorbed at the hot side of the TEM and will partly be converted into electric energy due to the Seebeck effect. The remaining Peltier heat is released at the cold side of the TEM, together with the transmitted Fourier heat. Under transient conditions, heat is stored into or released from components of the assembly, resulting in local variation of the Fourier heat flow. Concurrently, heat is transported under electric current flow from the hot to the cold side of a TEG module by the Peltier effect (Fig. 3), which is added to the Fourier heat and increases the effective total heat transport throughout the TEM compared to the open loop case.[41]

The Peltier heat at the hot and cold sides is not equal, due to differences of the absolute temperatures and the respective Seebeck coefficients. This implies for a thermoelectric generator module in the CPM that the Peltier heat at its hot side is higher than on its cold side, since the $S \cdot I \cdot T_H > S \cdot I \cdot T_C$. In the CPM case, the difference of Peltier heat is converted into electrical energy, which is only partly exported as electrical output power, P, outside of the TEM. The other part is lost along the thermoelectric legs as liberated Joule heat, $\dot{Q}_J$, of which half is transferred to the hot side and a half to the cold side of the TEM, as indicated per Fig. 3. If T_H and T_C of the heater and cooling plate, respectively, remain at pre-set temperatures during an increase of the electric current flow through the TEM, then T_5^h will drop and T_0^c will increase at the boundaries of the TEM (Fig. 3), since the Peltier heat flow through the TEM leads to additional Fourier heat flow through the outer components of the column such as HFM and thermal contact resistances and consequently to additional temperature drops across their thermal resistance. Therefore, under such conditions, the Peltier heat flow reduces the open loop voltage, V_o, by a decrease of the effective temperature difference across the TEM.

In order to get a quantitative estimate of how physical properties affect the local heat flow distribution in the transient case, it is necessary to solve the PDE of the heat transport within a TE leg. As a first step, a single passive block is considered in a 1D model. The solution of the temperature profile along the element from the governing heat balance equation is derived here for CPM

TABLE I. Boundary conditions and initial conditions for transient simulation of a homogeneous block.

Left BC	Right BC	Initial condition
$T(0,t) = \phi_1 = s \cdot t + \phi_0$	$T(L,t) = \phi_0$	$T(z,0) = \phi_0$

conditions under consideration of Fourier heat conduction and heat capacity. Therefore, this configuration (named case 1 here, with case 2 treating a conductive block with an electric current flow but no Seebeck effect) equals the situation of a block of material, e.g., an HFM, as shown in Appendix B. The boundary conditions are shown in Table I. The development of a transient measuring method requires the solution of the PDE under a transient boundary condition.

The transient boundary condition considered here is limited to a constant temperature drift applied to the left side (hot side) of the passive block with a drift rate s in Kelvin per second (rate of temperature change) and an initial locally constant temperature ϕ_0. Here, t is the time. At the cold side of the passive block, a constant in time temperature ϕ_0 is kept.

The transient Fourier equation without inner heat sources in a 1D model for case 1 [Eq. (7)] considers the local density of the heat capacity of the block $c\rho_m$ as well as its thermal conductivity κ,

$$c\rho_m \frac{dT}{dt} = \kappa \frac{d^2 T}{dz^2}. \tag{7}$$

Equation (7) shows that the amount of heat flow absorbed in a differential volume is equal to the change of the amount of Fourier heat transferred through the differential volume. To solve this PDE, the separation of variables technique[44] can be applied, resulting in the quasi-steady bilinear function $w_1(z,t)$,

$$w_1(z,t) = \phi_0 + st\left(1 - \frac{z}{L}\right). \tag{8}$$

Next, the non-homogenous function $v_1(z,t)$ can be chosen as an eigenfunction [Eq. (9)],

$$v_1(z,t) = \sum_{n=1}^{\infty} \widehat{v_n}(t) \sin(\lambda_n z), \tag{9}$$

where $\lambda_n = n\pi/L$. After expanding the eigenfunction,[45] the non-homogenous function is solved by consideration of the BCs and IC [Eq. (10)],

$$v_1(z,t) = \frac{2}{\pi^3} \frac{sL^2}{\alpha} \cdot \sum_{n=1}^{\infty} \frac{e^{-\alpha\left(\frac{n\pi}{L}\right)^2 t} - 1}{n^3} \cdot \sin\left(n\pi \frac{z}{L}\right), \tag{10}$$

where $\alpha = \kappa/c\rho_m$ is the thermal diffusivity. Introducing a time constant $\tau_1 = L^2/\alpha\pi^2$, Eq. (10) simplifies into

$$v_1(z,t) = \frac{2}{\pi} s\tau_1 \cdot \sum_{n=1}^{\infty} \frac{e^{-n^2 \frac{t}{\tau_1}} - 1}{n^3} \cdot \sin\left(n\pi \frac{z}{L}\right). \tag{10a}$$

Adding both the quasi-steady and non-homogenous functions gives the transient solution for case 1 [Eq. (11)] (Appendix C),

$$T_1(z,t) = w_1(z,t) + v_1(z,t)$$

$$= \phi_0 + st\left(1 - \frac{z}{L}\right) - \frac{2}{\pi}s\tau_1\sum_{n=1}^{\infty}\frac{1}{n^3}\sin\left(n\pi\frac{z}{L}\right)$$

$$+ \frac{2}{\pi}s\tau_1\sum_{n=1}^{\infty}\frac{e^{-n^2\frac{t}{\tau_1}}}{n^3}\sin\left(n\pi\frac{z}{L}\right). \quad (11)$$

Equation (8) does not include all terms that will not decay to zero with time. Instead, one of them is contained within Eq. (10), namely the stationary term related to the heat capacity of the block material [Eq. (12)],

$$\Delta T_{HC}(z) = \frac{2}{\pi}s\tau_1\sum_{n=1}^{\infty}\frac{1}{n^3}\sin\left(n\pi\frac{z}{L}\right). \quad (12)$$

For the mathematical solution of the PDE, the complete solution is composed of a homogeneous and an inhomogeneous solution [Eq. (11)]. However, for the physical analysis of the transient temperature profile, it is more adequate to split the solution into a quasi-stationary one (w_1'), which contains all constant and linearly time-dependent components, and a decay function (v_1'), of all rapidly decaying to zero constituents,

$$w_1'(z,t) = \phi_0 + st\left(1 - \frac{z}{L}\right) - \frac{2}{\pi}s\tau_1\sum_{n=1}^{\infty}\frac{1}{n^3}\sin\left(n\pi\frac{z}{L}\right), \quad (13)$$

$$v_1'(z,t) = \frac{2}{\pi}s\tau_1\sum_{n=1}^{\infty}\frac{e^{-n^2\frac{t}{\tau_1}}}{n^3}\sin\left(n\pi\frac{z}{L}\right). \quad (14)$$

Using the same BCs and IC but additionally involving a constant electric current flow that introduces a release of Joule heat along the block (case 2) will affect the temperature distribution and, therefore, the overall heat transport through an electrically conductive (but thermoelectrically inactive) block. This is considered in the heat balance PDE (15),

$$c\rho_m\frac{dT}{dt} = \kappa\frac{d^2T}{dz^2} + \rho j^2. \quad (15)$$

This function includes locally and timely constant Joule heating ρj^2. Likewise, going through the same steps as for case 1 leads to the transient temperature function for case 2 [Eq. (16)] (Appendix C),

$$T_2(z,t) = w_2'(z,t) + v_2'(z,t), \quad (16)$$

$$w_2'(z,t) = \phi_0 + st\left(1 - \frac{z}{L}\right) + 0.5\beta x(L - z) - \frac{2}{\pi}s\tau_1\sum_{n=1}^{\infty}\frac{1}{n^3}\sin\left(n\pi\frac{z}{L}\right), \quad (17)$$

$$v_2'(z,t) = \frac{2}{\pi}s\tau_1\sum_{n=1}^{\infty}\frac{e^{-n^2\frac{t}{\tau_1}}}{n^3}\sin\left(n\pi\frac{z}{L}\right) + \frac{2}{\pi^3}\beta L^2$$

$$\times\sum_{n=1}^{\infty}\frac{(\cos(n\pi) - 1)e^{-n^2\frac{t}{\tau_1}}}{n^3}\sin\left(n\pi\frac{z}{L}\right), \quad (18)$$

with $\beta = \rho j^2/\kappa$. In $v_2'(z,t)$, the first term is related to the heat capacity and the second to the Joule heat liberation. A polynomial fit of

$v_2'(z,t)$ over z can be used to plot accordingly the partial temperature profile for a given time and to determine its maximum along the block, v_{max}. This maximum of the temperature decay function $v_2'(z,t)$ is calculated at each time step of the simulation. Plotting v_{max} vs the simulation time for a defined $n = 100$ range gives a function decaying faster than its first term, which follows the law of $v_{max,1} = -A_{v,1}\exp(-t/\tau_1)$. Here, $A_{v,1} = \frac{2}{\pi}s\tau_1 - \frac{4}{\pi^3}\beta L^2$ is the maximum temperature offset amplitude at starting time. Note that both the amplitude and the relaxation of the heat capacity component of $v_2'(z,t)$ scale with the time constant τ_1 and that the amplitudes of all of $A_{v,1}$, $\Delta T_{HC}(z)$ and $\Delta T_J(z)$ [Eq. (20)] scale with L^2. The τ_1 value can serve to estimate when the rapidly decaying transient effects no longer affect the temperature profile of the block. Since the function $v_2'(z,t)$ decays toward zero, this means that after a certain period of a few τ_1 in duration, only the quasi-stationary solution $w_2'(z,t)$ will remain as the temperature distribution along the block. More specifically, in Eq. (17), there are three terms contributing to the overall temperature profile: related to transferred Fourier heat [Eq. (19)], released Joule heat [Eq. (20)], and heat capacity [Eq. (12)],

$$T_F(z,t) = \phi_0 + st\left(1 - \frac{z}{L}\right), \quad (19)$$

$$\Delta T_J(z) = 0.5\beta z(L - z). \quad (20)$$

The Fourier heat contribution is shown in Fig. 4(a), where the profile is linearly varying with location and is also linearly time dependent at each z. On the other hand, both the Joule heat [Fig. 4(b)] and heat capacity [Fig. 4(c)] contributions are not time dependent and vary only with location along the passive block. Moreover, the Joule heat will not change with the drift rate, unlike the heat capacity contribution. In detail, the Joule heat temperature profile $\Delta T_J(z)$ is a parabola with its maximum in the middle of the passive block and falling values toward the edges, while the heat capacity profile $\Delta T_{HC}(z)$ is an asymmetrical function with its peak located closer to the transient BC side and likewise falling to zero at both sides. The reason for the asymmetry in the heat capacity profile stems from the asymmetrical boundary condition. The quasi-stationary term $w_1'(z,t)$ [Eq. (13)], which can be approximated by a polynomial of third order, is the term that is left over after $v_1'(z,t)$ [Eq. (14)] decays to zero.

Method 2: Comparison of the analytical to a numerical model for idealized passive block and HFM

As a numerical counterpart for the analytical PDE solution, the validity of an OpenModelica (OM) CPM model [Fig. 5(a)] for case 1 (homogeneous block without current flow) is tested by comparison of the time-dependent temperature evolution at certain positions along the block. However, to be able to create a complete digital twin of the T-TEGMA as a next step, the inner temperature distribution in a passive block for the CPM case needs to be considered. Therefore, consideration of Joule heat liberation is included for the current-loaded case 2 as well [Fig. 5(b)]. In these calculations, the block was divided into five segments. The location of each temperature sampling point is indicated by $z = 0$–5 mm in 1 mm increments. Here, the discretization error will decrease with an increase in sampling points since the number of sampling points
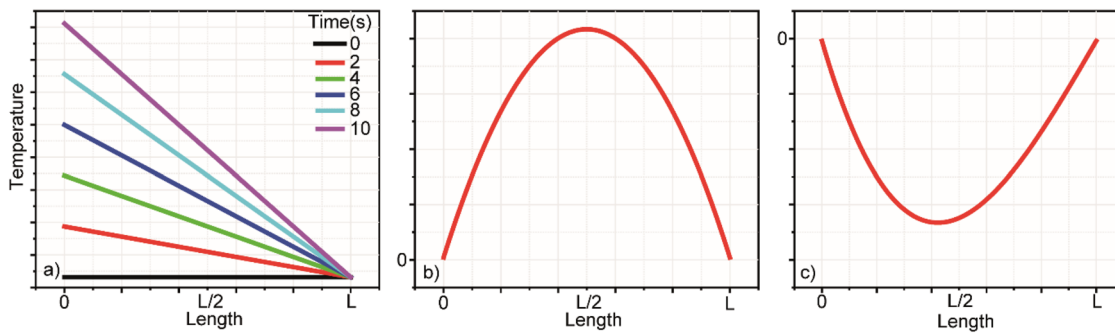
FIG. 4. Schematic example plots of the qualitative individual temperature profile contributions to the quasi-stationary solution [Eq. (17)], related to (a) transferred Fourier heat from the drifting side to the constant temperature side, $T_F(z, t)$, (b) Joule heat, $\Delta T_J(z)$, and (c) heat capacity, $\Delta T_{HC}(z)$. Note that both (b) and (c) contributions are constant in time. The values of (c) are negative for increasing boundary temperatures but positive for falling ones.

affects the approximation by the OM models. Nonetheless, because these OM models are CPM based, only a small deviation is expected in the quasi-stationary state since the local material properties do not change. In a temperature dependent properties model (TDPM), the difference would be greater due to the temperature dependence of the material properties, which would lead to local variation in material properties along the block.

The topological models in Figs. 5(a) and 5(b) follow the same boundary conditions as given in Table I. In these models, OM uses the specified material and physical properties (Appendix B) and assigns them to the sub-models representing equisized segments of the block. The segment sub-models in turn use the given temperature drift rate as well as material and device properties to compose the heat balance and temperature evolution along the block. The TRS segments contain a thermal resistance that determines the temperature drop along the block, while the TERS contain an additional electrical resistance that generates Joule heat and an ohmic voltage drop that is measured by the voltage sensor in Fig. 5(b). The OM model in Fig. 5 contains some conceptual inadequacies, with the first one being that heat absorbed by the HCS is based on the temperature drift at the hot side of the segment rather than of its middle. This means that the local temperature drift rate and with it the absorbed energy will be slightly overestimated against that of a real block, resulting in a little lowered temperature profile along the inner sensor points of the block than in reality. Furthermore, if the absorbed energy is extracted at the hot side of the segments but not symmetrically, then a higher than real inflowing heat flow will adjust. However, due to the BCs, this will not affect the temperature profile at the segment interfaces.

In an HFM, Joule heat does not apply as no current is flowing. Therefore, the PDE, which is solved for case 1, can be applied to the HFM by entering the BCs, s_{HFM}, geometry, L_{HFM}, and material properties, α_{HFM}, for the HFM in Eq. (11). Here, the time constant for the CSHFM is $\tau_2 = L_{HFM}^2/(\alpha_{HFM}\pi^2)$. The equation was implemented to compare the precision between the PDE solution and the OM model with increasing discretization with 5, 9, and 19 equisized segments, respectively, for a CSHFM block with a total length of 60 mm. Therefore, the segmentation of the CSHFM starts from the same relative segmentation of 20%, as it was already applied above

and uses the boundary conditions from Table I. This study serves to determine the required axial local discretization needed for sufficient accordance of results by OM-CPM and the PDE. From the results, an axial discretization of six segments was determined as the basis for creating an OM TDPM of the CSHFM under transient boundary conditions. This model is built from TRS and HSC components that can take as an input the average temperature between the segment sides to conclude on their temperature dependent c_{HFM} and κ_{HFM}.

As a next step, the OM-TDPM results were compared against the PDE-CPM solution and finite element modeling (FEM) software commonly used for thermal simulations. A 60 mm long CSHFM with a 40 × 40 mm² cross section was simulated in a transient ANSYS[46] model with 365 000 elements along the centerline of the CSHFM in the direction of heat flow. Due to the long computation time, it was limited to an experimental period of 44 s only, which is, however, sufficient for a comparative referencing of results obtained from OM-TDPM and PDE-CPM. To assess the impact of temporal discretization on the accuracy of the OM-TDPM and PDE-CPM, a comparison was made to the ANSYS model. ANSYS was executed using a baseline test at 1 ms, serving as a reference point. The performances of OM-TDPM and PDE-CPM were then compared at 1, 5, and 10 s to this baseline.

Method 3: Comparison between numerical modeling in a functional circuit model and experiment

Turning back to Eq. (6) for a TDPM model, $\dot{Q}_F$ contains a first order derivative with respect to the space coordinate of the heat flow, dT/dz, which can be locally approximated in the sense of the finite difference method (FDM)[47] by evaluation of temperature differences along the CSHFM block, measured over the segments between the thermocouples positioned along the centerline of the CSHFM with a distance of Δz between neighboring ones [Fig. 2(a)], effectively allowing for approximating mean local spatial derivatives by $\Delta T/\Delta z$. Theoretically, this approximate could be improved by increasing the number of sensor points along the CSHFM. However, such an increase might yield no improvement in measurement accuracy due to practical limitations that stem from the temperature resolution,
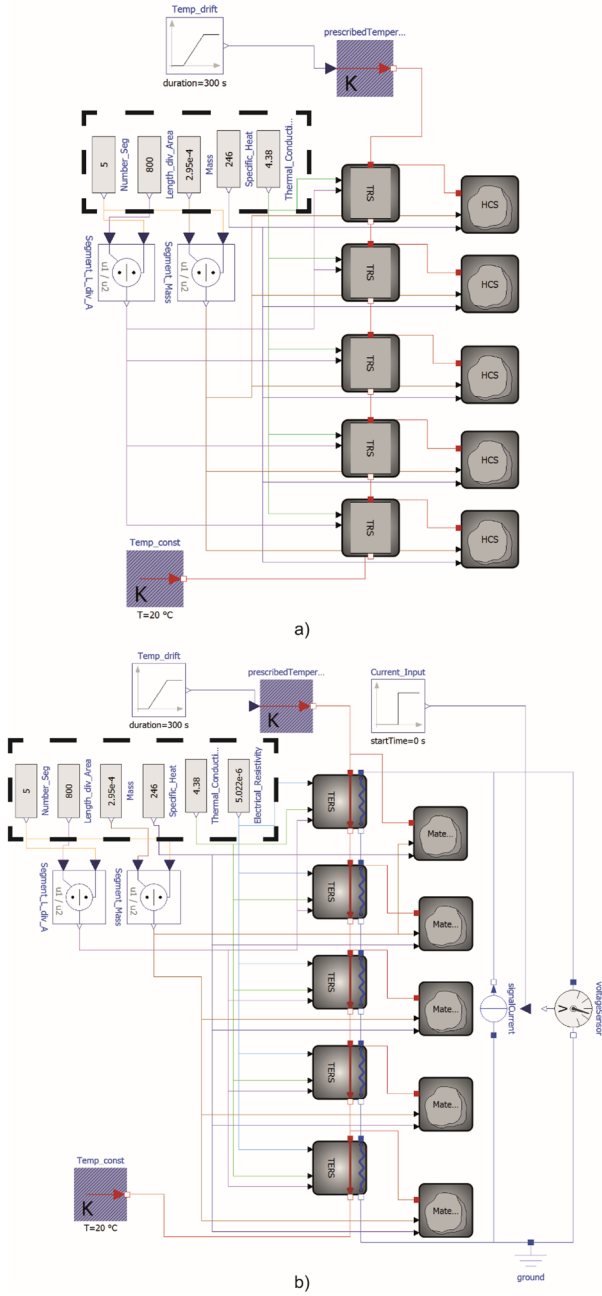
FIG. 5. (a) OM model including sub-models for representation of the heat capacity (HCS) and thermal resistance (TRS) per segment. (b) OM model including thermally and electrically resistive sub-models (TERS). The dashed square highlights control elements for setting the constant material and physical properties of the block.

signal noise, homogeneity of thermal sensor coupling, or manufacturing tolerances of sensor positions in the CSHFM. Further, the absorption rate of inner heat, $\dot{dU}$, contains a first order derivative but with respect to time, dT/dt, approximated by $\Delta T/\Delta t$, and is

experimentally related to the sampling rate. The implementation of an algorithm that calculates heat flow $\dot{Q}_F$ and local absorption $\dot{dU}$ at a common time t employs a temporal interpolation, deduced from temperature measurements at the positions z_i and z_{i+1} (Fig. 6), according to T_i^c and T_{i+1}^c (Fig. 2), respectively. In order to calculate the Fourier heat flowing between z_i and z_{i+1} with changing time (t_j, $j = 0, 1, 2, 3, \ldots$), the temperature gradient is found as follows:

$$T'\left(\frac{z_i + z_{i+1}}{2}, t_j\right) \approx \frac{\Delta T_{i,j}}{\Delta z} = \frac{T(z_{i+1}, t_j) - T(z_i, t_j)}{z_{i+1} - z_i}, \quad (21)$$

and

$$T'\left(\frac{z_i + z_{i+1}}{2}, t_{j+1}\right) \approx \frac{\Delta T_{i,j+1}}{\Delta z} = \frac{T(z_{i+1}, t_{j+1}) - T(z_i, t_{j+1})}{z_{i+1} - z_i}. \quad (22)$$

However, since this is an averaging procedure, the material properties [$\kappa_{HFM}(T)$] at an average temperature, at the middle position z_{i+} between z_{i+1} and z_i [substituting $z_{i+} = (z_{i+1} + z_i)/2$], both calculated at t_j and t_{j+1}, are used [Eqs. (23) and (24)],

$$T(z_{i+}, t_j) \approx \frac{T(z_i, t_j) + T(z_{i+1}, t_j)}{2}, \quad (23)$$

$$T(z_{i+}, t_{j+1}) \approx \frac{T(z_i, t_{j+1}) + T(z_{i+1}, t_{j+1})}{2}. \quad (24)$$

Equations (21)–(24) are then applied to find the Fourier heat flowing through the segment at t_j,

$$\dot{Q}_F(z_{i+}, t_j) = \kappa_{HFM}(T_{i+,j}) A_{HFM} T'(z_{i+}, t_j), \quad (25)$$

and at t_{j+1},

$$\dot{Q}_F(z_{i+}, t_{j+1}) = \kappa_{HFM}(T_{i+,j+1}) A_{HFM} T'(z_{i+}, t_{j+1}), \quad (26)$$

then to find the interpolated $\dot{Q}_F$ between t_j and t_{j+1} [with the substitution $t_{j+} = (t_j + t_{j+1})/2$],

$$\dot{Q}_F(z_{i+}, t_{j+}) = \frac{\dot{Q}_F(z_{i+}, t_j) + \dot{Q}_F(z_{i+}, t_{j+1})}{2}. \quad (27)$$

On the other hand, the rate of absorbed heat in each segment is calculated as a function of the temperature drift rate between t_j and t_{j+1} using Eq. (28) as follows:

$$\dot{T}(z_{i+}, t_{j+}) \approx \frac{\Delta T}{\Delta t} = \frac{T(z_{i+}, t_{j+1}) - T(z_{i+}, t_j)}{t_{j+1} - t_j}. \quad (28)$$

Furthermore, to calculate the c_{HFM} at (z_{i+}, t_{j+}), the average temperature between $T(z_{i+}, t_j)$ and $T(z_{i+}, t_{j+1})$ is calculated from Eqs. (23) and (24) as

$$T_{i+,j+} \approx \frac{T(z_{i+}, t_j) + T(z_{i+}, t_{j+1})}{2}. \quad (29)$$

As a result, the absorbed heat in the segment between z_i and z_{i+1} is calculated as

$$\dot{dU}_i(t_{j+}) = \Delta m_{HFM} c_{HFM}(T_{i+,j+}) \dot{T}(z_{i+}, t_{j+}). \quad (30)$$
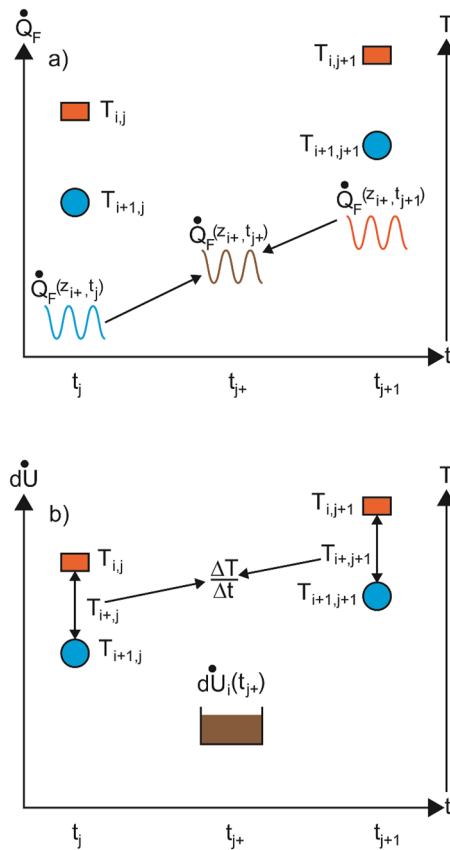
FIG. 6. Qualitative illustration of the TMF method for a transient heat flow measurement on a segment of the HFM with the definition of temperature and time steps for determination of the (a) Fourier heat flow, $\dot{Q}_F$, and (b) the absorption rate of inner heat, $\dot{dU}$. The orange rectangles and blue circles symbolize temperature measurements by the thermocouples T_i^c and T_{i+1}^c [Fig. 2(a)], respectively.

$\dot{Q}_F$ is measured with a sampling rate of 0.2 s^{-1} at $t_j = 5$ s and $t_{j+1} = 10$ s by the thermocouples T_0^c, T_1^c [see Fig. 2(a)], which define the first segment of the CSHFM [see Fig. 6(a)]. The determination of $\dot{dU}$ needs two temperature measurements separated by Δt to conclude on the approximation to dT/dt. Therefore, $\dot{Q}_F$ is interpolated from both readings.

The process of repeating temperature measurements and evaluations according to Eqs. (21)–(30) defines the TMF for determination of the heat flux and heat absorption rate as a function of time for individual segments of the HFM. Therefore, tests of the TMF procedure have been performed using a digital twin of the T-TEGMA, which is developed in OM [Fig. 7(a)] and in which a programmed routine (Fig. 8) simulates a temperature cycle in the T-TEGMA. This procedure can also be repeated over several temperature cycles. In particular, the time it takes the T_h at the TEG to go from 273 to 1073 K can be read from the simulation. The heating rate is varying in the beginning and then stabilizing. Dividing the overall

temperature increase by this time gives us a constant heating rate, s_{HFM}, which is entered into Eq. (11).

In accordance with the real T-TEGMA apparatus, the digital twin contains a multitude of components [Fig. 7(a)], which are involved in the simulation of the temperature evolution along the measurement column and particularly within the HFM. Every component is modeled by functional blocks, to which geometric and material properties can be assigned in accordance with pre-set material options. The TEM is modeled at this stage as a thermal dummy with only heat capacity and Fourier heat considered. Consequently, the model is one dimensional and is restricted only to heat conduction without consideration of convection or radiation. The CSHFM is modeled by $n = (5, 9, 19)$ serially connected blocks representing single CSHFM-segments, as defined by $n + 1$ thermocouple locations. The CSHFM segments are represented by sieving chain elements of thermal resistances and capacities that are offered as functional elements by OM. Every element carries information about the underlying physical properties and provides equations for the description of the thermal transport with respect to conduction of Fourier heat and heat absorption. Correspondingly, individual material properties are assigned to every element of the sieving chain either as functions varying with temperature or as static values for CPM. The temperatures T_0^c to T_5^c from these elements are used as the required input values for an implementation of Eqs. (21)–(30), which describe the TMF. The main difference between OM and the TMF is that OM can calculate the rate of absorbed heat per segment, $\dot{dU}$, directly at every time step instead of based on temperatures averaged over time [Eqs. (23) and (24)]. This implies that for comparison of results between OM and the simulated application of the TMF, the $\dot{dU}$ provided by OM needs to be averaged between two time steps in order to reference both values to the same $t = t_{j+}$, as used by the TMF [Eq. (30)].

RESULTS

Results and discussion 1: Comparison of PDE results to OM-CPM and decaying transient effects

A comparison of temperature profiles along the TE block (Appendix B) calculated by the PDE and OM is shown in Fig. 9. At a discretization into five segments, the maximum absolute temperature deviation for the entire simulation time is found for $I = 0$ A at $t = 0.3$ s and $z = 1$ mm, where $|T_{OM} - T_{PDE}| \approx 0.073$ K, i.e., negligibly small. These values are approximately halved for a comparative calculation with ten segments.

Results for case 2, which incorporates Joule heat generation [Eq. (16)], and comparing results from the PDE solution to the OM simulation [Fig. 5(b)] are shown in Fig. 9. There is an almost perfect agreement between results from OM and the PDE solution. Here, the downward convex temperature profile due to the heat capacity that is dominating at zero and low current will be overcompensated by the upward convex Joule-related temperature profile with increasing current. We observe a saturating temperature relaxation to the quasi-stationary profile in the inner regions of the block. After an initial period, the quasi-stationary state has been established, and all temperatures rise linearly with time.

The involvement of the Joule heat generation means that the quasi-stationary $w_2'(z, t)$ contribution to the temperature profile
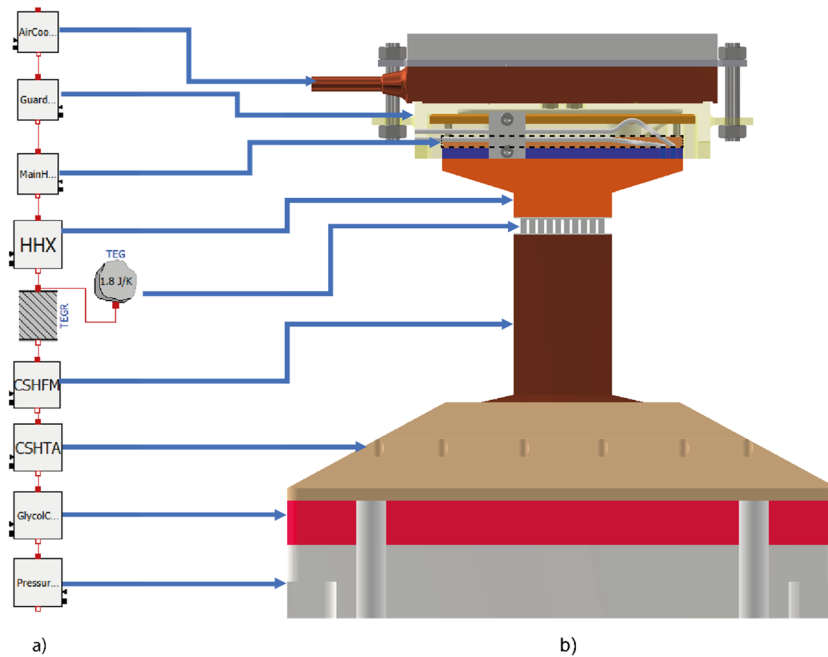
09 December 2024 11:36:47

FIG. 7. Schematic of functional elements of the OM model (a) representing components of the measuring section. The measuring section (b) is built by stacking of, from top to bottom: air cooled plate, guard heater and main heater, hot side heat exchanger (HHX), TEG represented in (a) by its heat capacity and its thermal resistance, CSHFM, cold side heat transfer adapter, cooled plate, and pressure load assembly.
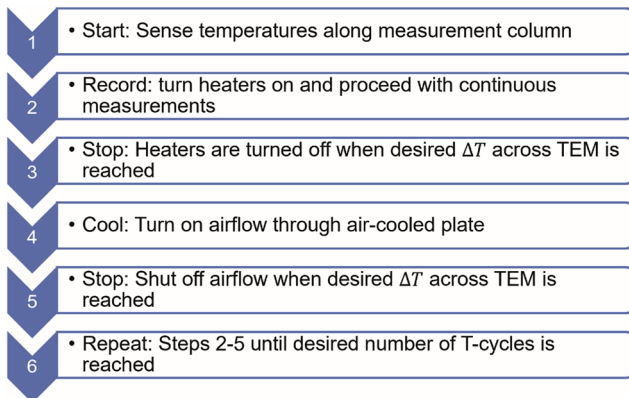
<div style="text-align: right">09 December 2024 11:36:47</div>

FIG. 8. Measuring procedure of the current OM T-TEGMA simulation. During the measuring procedure, the cold side of the cooled plate in Fig. 7 is maintained at constant temperature.

will contain a locally symmetric parabolic term, which appears as a temperature increase in the inner part of the block as shown by Figs. 9(d), 10(a), and 10(b). A slight asymmetry arises from the asymmetric heat absorption along the leg due to the heat capacity. The bow of the temperature profile has initially not yet evolved due to the constant initial condition. Mathematically, this is expressed

by the decay function $v_2'(z, t)$ plotted in Fig. 10(c) at different times. $v_2'(z, t)$ represents the deviation between the real transient temperature profile and the quasi-stationary transient profile. It is obvious that the part $v_2'(z, t)$ of the transient profile is temporary and decays toward zero within a few time constants. After a time of 4.5 τ_1 this contribution falls below 1% of its original value, where τ_1 indicates its relaxation time, the time at which the first and largest and slowest decaying term of the sum forming $v_2'(z, t)$ decays to 1/e, i.e., to 36.8% of the original amplitude. After a time of 4–5 τ_1, the quasi-stationary temperature profile dominates under transient BCs. It is essential to note that such small relaxation times apply to the geometry of the 5 mm short passive block of Appendix B and would be longer in longer blocks and much longer in a multi-component measuring section such as the one shown in Fig. 7.

In Fig. 9(a), the shape of the plot shows slight left-hand curvature of the temperature profiles, indicating a delay in the temperature increase of the inner regions of the sample. This delay is due to the energy absorbed by the block in agreement with the heat capacity models in OM [Fig. 5(a)] and expressed by specific heat c and mass density ρ_m contained in the thermal diffusivity parameter α in the PDE solution [Eqs. (11) and (16)]. The difference in the curvature between Fig. 9(a) and Figs. 9(b)–9(d) is a result of the Joule heat generated by the electric current in the TERS model in Fig. 5(b), expressed by the term ρj^2 in the β variable of the PDE solution [Eq. (16)]. As seen in Fig. 10(c), the decay function contribution to the temperature is not symmetric along the TE block.
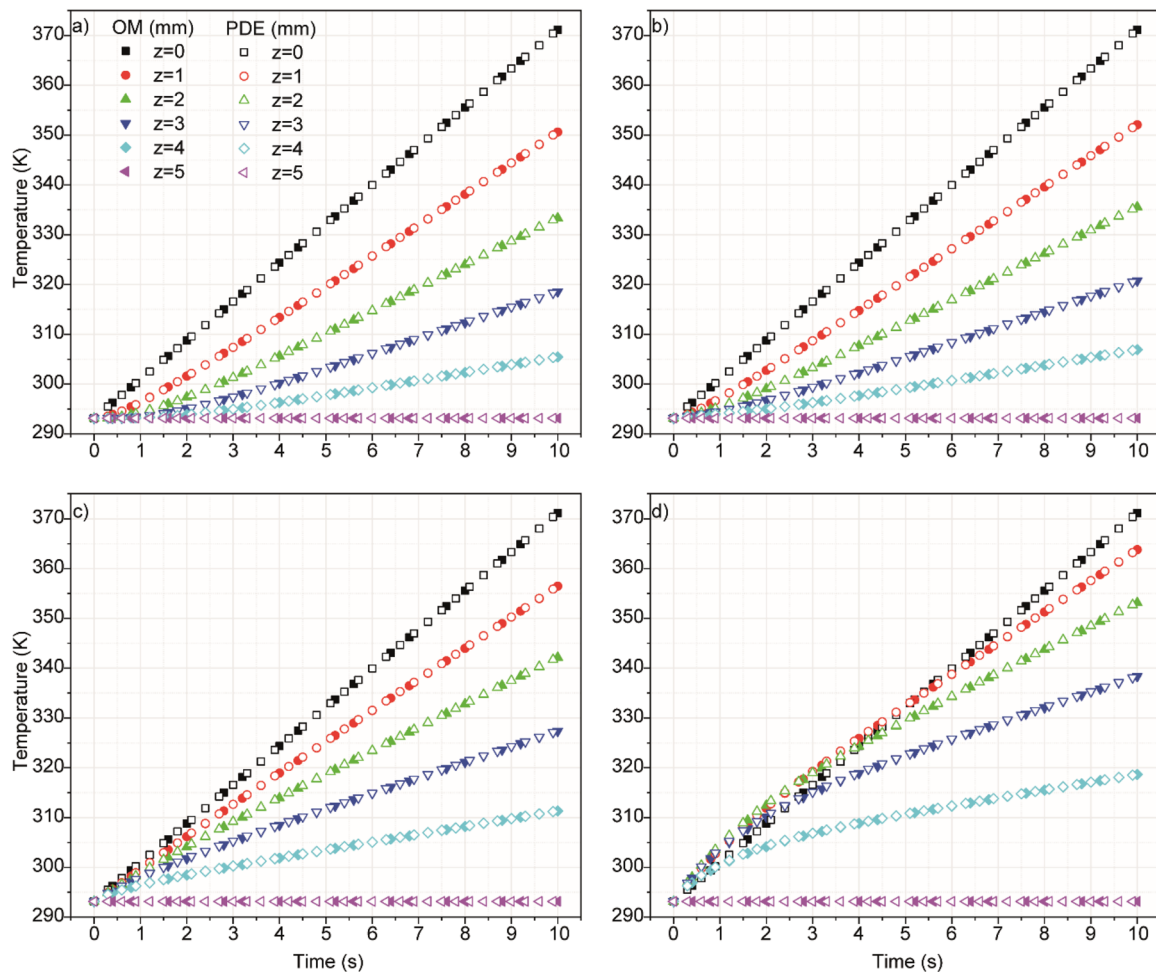
FIG. 9. Comparison of OM vs PDE evolution of transient temperature profiles along a passive block of 5 mm in length discretized into five segments. Effect of Joule heat generation for various electrical current values (a) 0 A, (b) 5 A, (c) 10 A, and (d) 15 A. Joule heat causes an increase in the temperature drift rate during a starting period that, for higher current values, overcompensates an initially lowered rate caused by the heat capacity.

This is due to the heat capacity term as the temperature drift rate is varying along the block.

Results and discussion 2: Validation of the HFM model

A discretization study considering the deviation between temperature profiles simulated in the OM and PDE models reveals that a 73 mm long CSHFM discretized into five segments has a very small absolute maximum temperature difference of $<5 \cdot 10^{-3}$ K, with the absolute difference decreasing to $<2 \cdot 10^{-3}$ and $<1 \cdot 10^{-3}$ K for an increasing discretization of 9 and 19 segments, respectively. This means that with an axial discretization of five segments, a CSHFM OM-CPM can, with high accuracy, reproduce the temperature evolution of an PDE-CPM equation. The question that naturally arises is whether an OM simulation of the CSHFM with TDPM

can accurately conclude on the temperature evolution of a physical HFM.

To answer this question, the temperature result of a FEM simulation in ANSYS with TDPM is compared in Fig. 11 with the outcome of an OM-TDPM. The FEM and OM TDPM simulations used full temperature dependent properties with different local discretizations of the models, whereas the PDE made use of constant properties, which have been determined from temperature averages according to the Ioffe formula (Appendix B) for all material properties except for the heat capacity. The maximum heat capacity value within the temperature range was chosen for the PDE-CPM model to consider a worst case of temperature deviation compared to the TDPM. In Fig. 7, the heating rate applied along the measurement column is derived from the testing procedure in Fig. 8. The temperature decreases from top to bottom of the column due to the thermal resistances and heat capacity of the components.
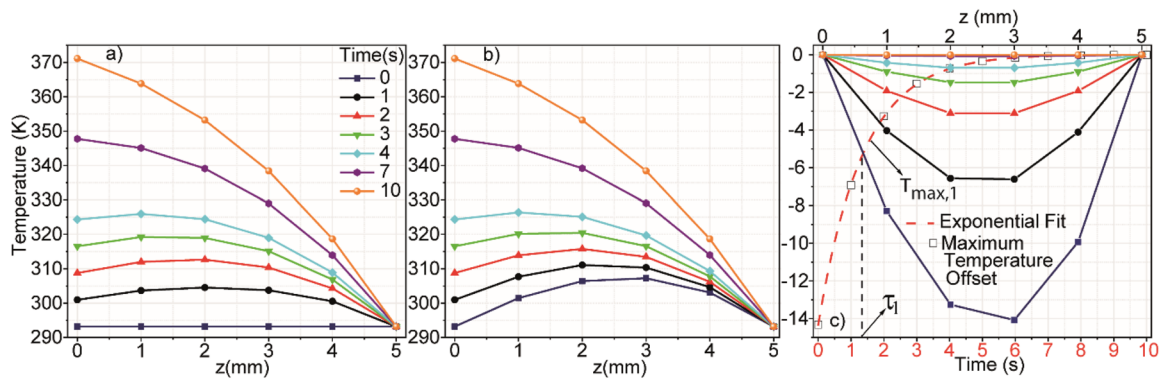
FIG. 10. Temperature profiles along the block according to the PDE solution with Joule heat generation by a current of 15 A at different times after the start of the transient BC according to Eq. (16). (a) full $T_2(z,t)$ evolution (b) quasi-stationary contribution $w_2'(z,t)$ according to Eq. (17) (c) decaying part given by the time-dependent decay function $v_2'(z,t)$ (top axis) according to Eq. (18). The plot shows additionally the time-dependent decay of the first (and slowest decaying) term of the maximum temperature offset $T_{max,1} = -14.3\,\mathrm{K}\exp(-t/\tau_1)$ (bottom axis; see Method 1) and indicates the time constant $\tau_1 = 1.36$ s.

At the hot side of the passive block (TEG, top BC), the heating rate is 7.8 K/s, and it drops to 0.107 K/s at the cold side (bottom BC) of the passive block, which is the top BC of the CSHFM. The bottom temperature BC of the CSHFM is held constant at room temperature. This rate is applied to all models in Fig. 11. This rate turned out to be practically useable for real measurements as it joins short measurement duration to still moderate transient effects. A higher heating rate at the top side of the passive block (TEG) will lead to stronger transient effects. Therefore, to make the CSHFM model applicable to the hot side HFM (HSHFM), a modified model approach is needed with a two-side drifting BC that can be deduced from the PDE-CPM. The decaying absolute temperature difference between the employed models is evaluated in the middle of the CSHFM at 30 mm distance from its boundaries according to $\left|\mathrm{T_{OM/TPDM}} - \mathrm{T_{FEM/TDPM}}\right|/\Delta T_{\mathrm{Total,A}}$, where $\Delta T_{\mathrm{Total,A}}$ equals the total temperature difference at a specific time, which is derived from the FEM-TDPM simulation. Figure 11 reveals a maximum temperature deviation between FEM-TDPM and the other models of about 2.67% at $t = 1$ s. However, the deviation between OM and FEM-TDPM decays quickly and stabilizes after 15 s to around 0.18% of $\Delta T_{\mathrm{Total,A}} = 1.9265$ K, which equals $3.47 \cdot 10^{-3}$ K. This is in good agreement with the maximum temperature difference $<5 \cdot 10^{-3}$ K, which was observed for the OM model with five segments according to the conducted discretization study. All results agree to a high level with each other. Furthermore, since the TMF is expected to be used after 4–5 fold relaxation time, which for the 60 mm CSHFM with $\tau_1 = 3.61$ s means that up to about 15 s the decaying transient effects have vanished and quasi-stationary conditions take over. Therefore, we cannot take any evaluation involving a quasi-stationary assumption in this period as we would in a physical HFM measurement. Due to the temperature-dependent properties used in FEM-TDPM and the high local discretization of this model, the results of the FEM-TDPM simulation can be considered the most accurate representation of the physical behavior of the CSHFM. Except for the initial period with non-quasi-stationary conditions, all models delivered a sufficiently good accordance to each other. Therefore, it is
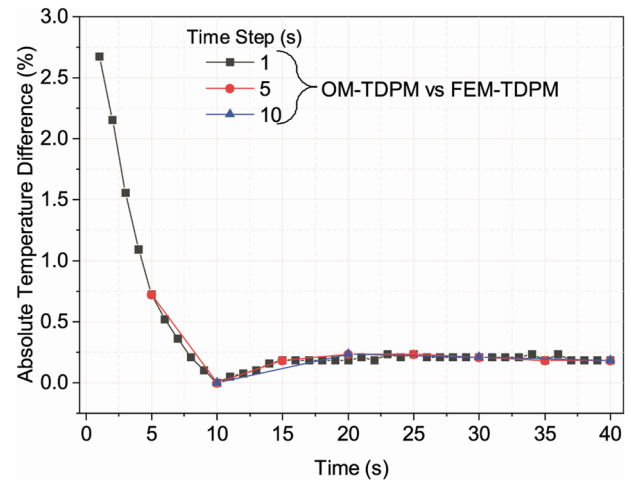

FIG. 11. Comparison of the temperature calculation accuracy at the 30 mm position of the CSHFM over time for time discretization steps of $\Delta t = 1$, 5, and 10 s in the OM. The FEM-TDPM was accomplished with temperature-dependent material properties and a time step $\Delta t = 1$ ms.

clear for the OM-TDPM that a temporal discretization of ~10 s and a spatial discretization of at least five segments used for a CSHFM will deliver sufficient accuracy. To summarize, Fig. 11 shows the resulting deviations of the temperature and gives high confidence in the accuracy of not only the OM-TDPM solution but also the PDE-CPM.

During the actual test of the T-TEGMA, the transient effects of the Joule and heat capacity portion in v_2', which leads to most of the error, will last only for a short period of time at the beginning of each heating sequence. Waiting a period of 4–5 time constants after the start of each test helps to take valid temperature measurements during the quasi-stationary time domain only.

Results and discussion 3: Comparison between OM CSHFM and simulated TMF

Having shown above that OM can accurately simulate the temperature evolution of the CSHFM, it is important to see also how the TMF can be used to determine local heat flux and heat absorption $\dot{U}$ based on the local temperature profiles of the temperature sensing points of an HFM. Therefore, the CSHFM is divided into six segments and simulated as a TDPM with a 5 s time step, which is in the order of the time constant. The full column of the TEGMA digital twin was involved in the simulation here, including the heater, HSHFM, TEG module CSHFM, and a cold side heat transfer adapter on a cooling plate (Fig. 7). From the temperatures virtually measured by OM at each of the sensing points, the stored thermal power is calculated [Eqs. (21)–(30)]. The heat absorption in the segments [Eq. (30)] is compared between OM and the TMF in Fig. 12. The transmitted Fourier heat [Eq. (27)] was found to be identically the same for both the calculated values by the CSHFM simulation in OM and those calculated by the simulated TMF.

Figure 12(a) shows a very good accordance between the absorbed heat rate obtained from the OM-TDPM model and the simulated application of the TMF. The actual difference in the values is highlighted for segment 3 in Fig. 12(b), showing that between 0 and 50 s the difference is quickly decaying below 1%. As indicated by the left axis of Fig. 12(b), the initially high deviation is a consequence of the non-linear temperature evolution in the inner parts of the measuring section (Fig. 7) violating the required quasi-stationary conditions. This corresponds to a timely varying heating rate in the CSHFM as a transient response to the temperature change at its boundaries that follow the relaxation behavior of the whole column. The variation in heating rate is most pronounced at the start of the transient process. This characteristic is amplified by the fact that the heater is controlled initially in a constant power mode rather than at

constant temperature drift. Although this does not cause an essential difference in a later phase of the measurement, it greatly affects the initial relaxation behavior. When the heater activates (Fig. 7), its power is initially absorbed by a small upper section of the measuring column, since the initial temperature profile during the early relaxation phase, is steep close to the heater but flat close to the sink. Accordingly, the temperature drift near the hot side of the column will be higher initially but will reduce when more and more parts of the column participate in the temperature rise and contribute to heat absorption from a heat source operating at constant power. In the inner parts of the column, this leads after a quick initial rise from zero to a more or less pronounced peak in the temperature drift rate (Fig. 13) and hence of the absorbed power as observed in Fig. 12(a). The effect is more intense for components closer to the heater but diminishes with increasing distance from the heater. Accordingly, in Fig. 12(a), the peak decreases in the colder segments and vanishes close to the cold side of the HFM. In conclusion, the rapid drop to small relative deviations as shown in Fig. 12(b) indicates the applicability of the TMF and a high accuracy of its heat flow determination soon after the variation of the temperature drift has calmed down. The TMF provides accurate results once the BCs at their hot and cold sides approximate a moderate, little varying temperature drift rate, which is reached here after about 50 s. For the understanding of the dynamic behavior, it is essential that there is a large difference between the time constants of a separate passive leg (Fig. 5)—here in the role of the CSHFM—and the whole measuring column of the T-TEGMA surrounding it (Fig. 7). For the separate CSHFM block, the time constant τ_1 is 3.61 s, while, as seen in Fig. 12(a), the time constant of the whole column is in the order of several hundreds of seconds. Note that the slow relaxation observed for segments 1–6 in Fig. 12(a) does only negligibly reflect the transient behavior of the CSHFM itself but is mainly governed by the temperature drift rates at its faces. Their slow change after the initial phase of 50 s is related to the slow relaxation of the measuring
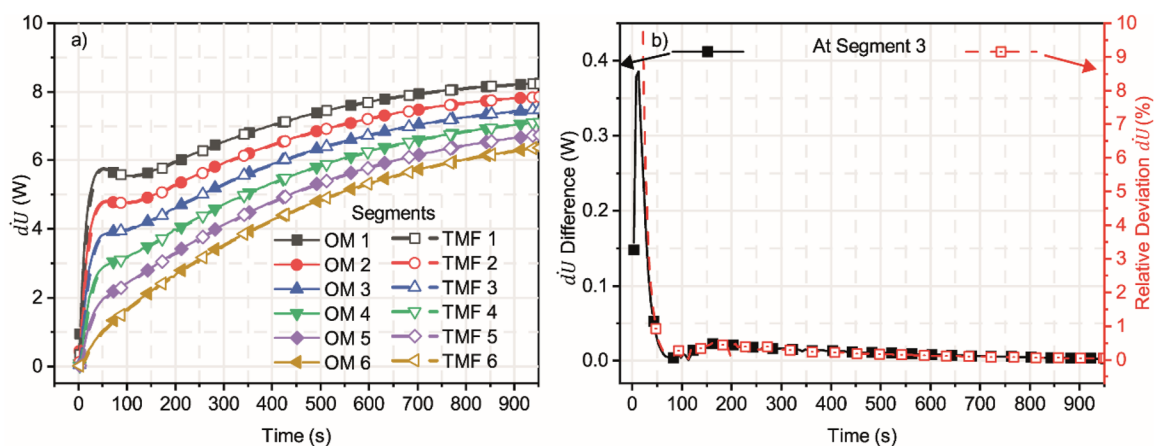
FIG. 12. The rate of heat absorption per segment is compared for six segments of an HFM using the simulated data from (a) OM-TDPM and the simulation of the TMF [Eq. (30)] with a time step of $\Delta t = 5$ s. The full column of the TEGMA digital twin was involved in the simulation here, with the HFM located at the cold side of the TEM. The small difference between OM and TMF is plotted in (b) for segment 3. Here, the temperature T_c on the CSHFM drifted from 293 to 403 K while T_C drifted from 293 K to about 353 K [Figs. 2(a) and 2(b)].
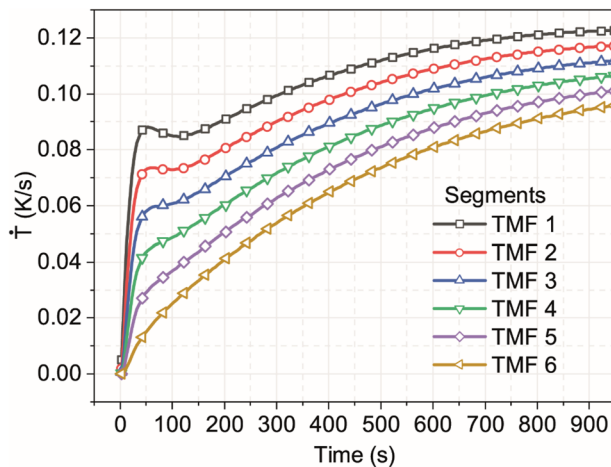
FIG. 13. Temperature drift rate for each segment [Eq. (28)].

column to its quasi-stationary state. According to its high weight and high thermal resistance, the relaxation time of the whole column is two orders of magnitude larger than that of the CSHFM. This, consequently, means that the CSHFM is practically already in quasi-stationary equilibrium internally during most of the relaxation phase of the whole column, which lasts over nearly 1000 s as read from Fig. 12(a) until the local temperature drift rates saturate, as an indication of reaching the quasi-stationary state. The reason for the slow relaxation depicted in Fig. 12(a) is that the underlying simulation includes the whole measuring column but not the separated HFM block alone, as in the two examples above. Estimating a system time constant with a total length of the column of 113 mm and assuming identical κ_{HFM} and c_{HFM} values gives a τ_1 value of 200–250 s. This coincides well with the system time constant depicted in Fig. 12(a).

Sufficient accuracy of the TMF is going to be achieved after a waiting time, which is governed by the component time constant of the HFM, which is much smaller than the system time constant. The deviation from quasi-stationarity is represented by the magnitude of the time-dependent decay function $v_1'(z,t)$, which is linearly scaling with the effective heating rate s [Eq. (14)]. As can be seen from Fig. 12(a), the absorbed energy per time $\dot{U}$ changes continuously over time and is different for every segment of the CSHFM. The effect of the temperature dependence of the specific heat on its variation is negligible, since its variation is less than 2% overall over the entire time interval (see Appendix B, Fig. 5). The variation of $\dot{U}$ thus essentially follows the variation of temperature drift rates $\dot{T} = \Delta T/\Delta t$ of the segments of the CSHFM, as plotted in Fig. 13.

Since every change of the temperature drift rate initiates transient decaying contributions to the temperature function of an HFM, the question arises to which extent a remaining magnitude of the decay function, i.e., a permanent slow change of the BCs to the HFM, will introduce uncertainty to the determination of heat flow, particularly within a time regime that is smaller than the system time constant. Therefore, the temperature drift rate becomes rather small after about 100 s, which indicates a minor contribution of the decay

function to the temperature profile along the CSHFM, which will reduce more and more with the stabilization of the temperature drift. This is in accordance with the negligible values and slow decay of the remaining deviation between OM simulation and TMF virtual measurements [Fig. 12(b)].

Although not perfectly quasi-stationary conditions are achieved with a permanent slow variation of the temperature drift rate, the impact of a remaining magnitude of the HFM decay function on the accuracy of the TMF will be negligible under the simulated conditions. Therefore, the TMF will provide reliable experimental values for absorbed energy and heat flow, and when combined with the measurement of electric power output (which on its own will need adequate correction for the transient conditions), also yield valid TEM module efficiency data [Eq. (1)].

CONCLUSION

A one-dimensional model approach to heat flow determination under transient temperature boundary conditions of a heat flow meter (HFM) used in thermoelectric module (TEM) characterization was introduced, neglecting any lateral heat loss due to convection or radiation. A transient measurement function (TMF) was developed and simulated in OpenModelica (OM) assuming Dirichlet boundary conditions of constant temperature drift. The benefit of such modeling is that it can derive experimental requirements for sensor instrumentation, signal sampling, and control of boundary conditions (BCs), e.g., the heating rate. However, most TEMs operate in steady state conditions; therefore, a transient measurement method introduces the central question of the relation between steady state properties and measurement results under transient conditions. One part of this answer is to consider the time constant, τ_1, after which the transient effects of the initial quick decay toward a quasi-stationary temperature profile no longer affect the temperature evolution of a passive block. The contribution of the initial, rapidly decaying function to the overall temperature profile decreases to below 1% after 4–5 τ_1, whereas after this time the analytically simple quasi-stationary temperature profile can be used as a base for a measurement recipe. However, the time constant is significantly larger in a complete thermoelectric generator measurement apparatus (T-TEGMA) model due to the larger mass and device length involved, compared to the HFM block alone. These relaxation times are governing the required waiting time required before valid results can be expected from transient heat flow characterization to establish quasi-stationary conditions. The time dependent partial differential equation (PDE) of a passive block with a constant properties model (CPM) and Joule heat production was solved and also modeled in OM. Both the PDE solution and the OM model provide consistent results showing a high degree of fidelity. Consequently, an OM temperature dependent properties model (TDPM) vs an FEM-TDPM in ANSYS were compared, confirming an almost ideal coincidence of results. Finally, an OM-TDPM of the CSHFM was taken for a comparison to the TMF simulation in OM. It was shown that the absorbed energy at each segment of the CSHFM due to its heat capacity was determined in accordance with the OM model by the simulated application of the TMF to a virtual implementation of the TEGMA measurement column (digital twin), which

gives access to the experimental determination of heat flow under transient temperature conditions.

SUPPLEMENTARY MATERIAL

Appendix A lists the abbreviations and variables in the paper as well as in the Appendixes. Appendix B provides material and geometric information used in the comparison of the analytical model to the numerical model for the idealized passive block and HFM. Appendix C provides a detailed mathematical derivation of the PDE for cases 1 and 2 of the passive block.

ACKNOWLEDGMENTS

AUTHOR DECLARATIONS

Conflict of Interest

The authors have no conflicts to disclose.

Author Contributions

Jhonatan Samuel Ferrer Caro: Formal analysis (equal); Funding acquisition (equal); Investigation (lead); Methodology (equal); Project administration (equal); Software (lead); Validation (lead); Visualization (lead); Writing – original draft (lead). **Eckhard Müller**: Conceptualization (supporting); Funding acquisition (equal); Project administration (supporting); Writing – review & editing (supporting). **Pawel Ziolkowski**: Conceptualization (lead); Methodology (equal); Project administration (lead); Supervision (lead); Validation (supporting); Writing – review & editing (lead).

DATA AVAILABILITY

The data that support the findings of this study are available from the corresponding author upon reasonable request.

REFERENCES

[1] A. F. Ioffe, L. S. Stil'bans, E. K. Iordanishvili, T. S. Stavitskaya, A. Gelbtuch, and G. Vineyard, "Semiconductor thermoelements and thermoelectric cooling," Phys. Today **12**(5), 42 (1959).

[2] K. Zabrocki, C. Goupil, H. Ouerdane, Y. Apertet, W. Seifert, and E. Müller, "Continuum theory of TE elements," in *Continuum Theory and Modeling of Thermoelectric Elements* (John Wiley & Sons, Ltd., 2016), pp. 75–156.

[3] H. J. Goldsmid, *Application of Thermoelectricity* (Butler and Tanner Ltd., 1960), p. 113.

[4] K. F. Hsu, S. Loo, F. Guo, W. Chen, J. S. Dyck, C. Uher, T. Hogan, E. K. Polychroniadis, and M. G. Kanatzidis, "Cubic AgPb$_m$SbTe$_{2+m}$: Bulk thermoelectric materials with high figure of merit," ChemInform **35**, 818–821 (2004).

[5] X. Shi, J. Yang, J. R. Salvador, M. Chi, J. Y. Cho, H. Wang, S. Bai, J. Yang, W. Zhang, and L. Chen, "Multiple-filled skutterudites: High thermoelectric figure of merit through separately optimizing electrical and thermal transports," J. Am. Chem. Soc. **133**(20), 7837–7846 (2011).

[6] G. Joshi and B. Poudel, "Efficient and robust thermoelectric power generation device using hot-pressed metal contacts on nanostructured half-Heusler alloys," J. Electron. Mater. **45**(12), 6047–6051 (2016).

[7] Q. Zhang, J. Liao, Y. Tang, M. Gu, C. Ming, P. Qiu, S. Bai, X. Shi, C. Uher, and L. Chen, "Realizing a thermoelectric conversion efficiency of 12% in bismuth telluride/skutterudite segmented modules through full-parameter optimization and energy-loss minimized integration," Energy Environ. Sci. **10**(4), 956–963 (2017).

[8] P. Jood, M. Ohta, A. Yamamoto, and M. G. Kanatzidis, "Excessively doped PbTe with Ge-induced nanostructures enables high-efficiency thermoelectric modules," Joule **2**(7), 1339–1355 (2018).

[9] H. Iwasaki, S. Yokoyama, T. Tsukui, M. Koyano, H. Hori, and S. Sano, "Evaluation of the figure of merit of thermoelectric modules by harman method," Jpn. J. Appl. Phys., Part 1 **42**(6A), 3707 (2003).

[10] A. De Marchi and V. Giaretto, "The elusive half-pole in the frequency domain transfer function of Peltier thermoelectric devices," Rev. Sci. Instrum. **82**(3), 034901 (2011).

[11] C. Goupil, H. Ouerdane, K. Zabrocki, W. Seifert, N. F. Hinsche, and E. Müller, "Thermodynamics and thermoelectricity," in *Continuum Theory and Modeling of Thermoelectric Elements* (John Wiley & Sons, Ltd., 2016), pp. 1–74.

[12] B. Ryu, J. Chung, and S. Park, "Thermoelectric degrees of freedom determining thermoelectric efficiency," iScience **24**(9), 102934 (2021).

[13] E. Groβ, M. Riffel, and U. Stöhrer, "Thermoelectric generators made of FeSi$_2$ and HMS: Fabrication and measurement," J. Mater. Res. **10**(1), 34–40 (1995).

[14] E. Müller, J. U. Bruch, and J. Schilz, "TE generator test facility for low resistance single elements," *Proceedings ICT98 (Cat. No.98TH8365)* (IEEE, 1998), pp. 441–444.

[15] H. Takazawa, H. Obara, Y. Okada, K. Kobayashi, T. Onishi, and T. Kajikawa, "Efficiency measurement of thermoelectric modules operating in the temperature difference of up to 550 K," in *2006 25th International Conference on Thermoelectrics* (2006), pp. 189–192.

[16] J. D. König, U. Nussel, M. Bartel, and U. Vetter, "Complete thermoelectric generator performance measurement," MRS Proc. **1218**, 410 (2009).

[17] E. A. Man, E. Schaltz, L. Rosendahl, A. Rezaniakolaei, and D. Platzek, "A high temperature experimental characterization procedure for oxide-based thermoelectric generator modules under transient conditions," Energies **8**(11), 12839–12847 (2015).

[18] H. Wang, W. Porter, H. Böttner, J. König, L. Chen, S. Bai, T. M. Tritt, A. Mayolet, J. Senawiratne, C. Smith, F. Harris, P. Gilbert, J. Sharp, J. Lo, H. Kleinke, and L. Kiss, "Transport properties of bulk thermoelectrics: An international round-robin study, part II: Thermal diffusivity, specific heat, and thermal conductivity," J. Electron. Mater. **42**, 1073 (2013).

[19] H. Wang, W. Porter, H. Bottner, J. König, L. Chen, S. Bai, T. M. Tritt, A. Mayolet, J. Senawiratne, C. Smith, F. Harris, P. Gilbert, J. Sharp, J. Lo, H. Kleinke, and L. Kiss, "Transport properties of bulk thermoelectrics—An international round-robin study, part I: Seebeck coefficient and electrical resistivity," J. Electron. Mater. **42**, 654 (2013).

[20] P. Ziolkowski, R. Chetty, P. Blaschkewitz, M. Ohta, A. Yamamoto, and E. Müller, "Interlaboratory testing for high-temperature power generation characteristics of a Ni-based alloy thermoelectric module," Energy Technol. **8**(11), 2000557 (2020).

[21] H. Wang, S. Bai, L. Chen, A. Cuenat, G. Joshi, H. Kleinke, J. König, H. W. Lee, J. Martin, M.-W. Oh, W. D. Porter, Z. Ren, J. Salvador, J. Sharp, P. Taylor, A. J. Thompson, and Y. C. Tseng, "International round-robin study of the thermoelectric transport properties of an *n*-type half-Heusler compound from 300 K to 773 K," J. Electron. Mater. **44**(11), 4482–4491 (2015).

[22] H. Wang, M. I. Fedorov, A. A. Shabaldin, P. P. Konstantinov, and G. J. Snyder, "Comparison of thermoelectric transport measurement techniques using n-type PbSe," J. Electron. Mater. **44**(6), 1967–1971 (2015).

[23] X. Hu and A. Yamamoto, "Characterization of thermoelectric conversion for a stacked leg with parasitic heat radiation," Measurement **171**, 108846 (2021).

[24] H. Armstrong, M. Boese, C. Carmichael, H. Dimich, D. Seay, N. Sheppard, and M. Beekman, "Estimating energy conversion efficiency of thermoelectric materials: Constant property versus average property models," J. Electron. Mater. **46**(1), 6–13 (2017).

[25] J. Mackey, F. Dynys, and A. Sehirlioglu, "Uncertainty analysis for common Seebeck and electrical resistivity measurement systems," Rev. Sci. Instrum. **85**(8), 085119 (2014).

[26] E. Lenz, F. Edler, and P. Ziolkowski, "Traceable thermoelectric measurements of Seebeck coefficients in the temperature range from 300 K to 900 K," Int. J. Thermophys. **34**(10), 1975–1981 (2013).

[27] A. Jacquot, H.-F. Pernau, J. König, U. Nussel, M. Bartel, and M. Jaegle, "Measurement uncertainties in thermoelectric research," in *8th European Conference on Thermoelectrics* (Como, 2010).

[28] C. Miers and A. Marconnet, "Uncertainty quantification for a high temperature Z-meter characterization system," in *2018 17th IEEE Intersociety Conference on Thermal and Thermomechanical Phenomena in Electronic Systems (ITherm)* (IEEE, 2018), pp. 572–581.

[29] Thermogeneratorcharakterisierung - Grundlagen und Begriffe.

[30] Thermogeneratorcharakterisierung charakterisierung planarer TEM.

[31] P. Ziolkowski, P. Blaschkewitz, and E. Müller, "Heat flow measurement as a key to standardization of thermoelectric generator module metrology: A comparison of reference and absolute techniques," Measurement **167**, 108273 (2021).

[32] *Continuum Theory and Modeling of Thermoelectric Elements*, 1st ed., edited by C. Goupil (Wiley, 2016).

[33] J. Holman, "Introduction," in *Heat Transfer*, 10th ed., edited by J. Holman and J. Lloyd (McGraw-Hill, New York, 2002), pp. 1–20.

[34] P. Fritzson, A. Pop, K. Abdelhak, A. Ashgar, B. Backmann, W. Braun, D. Bouskela, R. Braun, L. Buffoni, F. Casella, R. Castro, R. Franke, D. Fritzon, M. Gebremedhin, A. Heuerman, B. Lie, A. Mengist, L. Mikelsons, K. Moudgalya, L. Ochel, A. Palanisamy, V. Ruge, W. Schamai, M. Sjölund, B. Thiele, J. Tinnerholm, and P. Östlund, "The OpenModelica Integrated environment for modeling, simulation, and model-based development modeling," Modeling, Identification and Control **41**(4), 241–295 (2020).

[35] D. Champier, "Thermoelectric generators: A review of applications," Energy Convers. Manage. **140**, 167–181 (2017).

[36] H. Jouhara, A. Żabnieńska-Góra, N. Khordehgah, Q. Doraghi, L. Ahmad, L. Norman, B. Axcell, L. Wrobel, and S. Dai, "Thermoelectric generator (TEG) technologies and applications," Int. J. Thermofluids **9**, 100063 (2021).

[37] T. C. Harman, "Special techniques for measurement of thermoelectric properties," J. Appl. Phys. **29**(9), 1373–1374 (1958).

[38] D. M. Rowe, *CRC Handbook of Thermoelectrics* (CRC Press, Boca Raton, FL, 1995).

[39] B. Kwon, S.-H. Baek, S. Keun Kim, and J.-S. Kim, "Impact of parasitic thermal effects on thermoelectric property measurements by Harman method," Rev. Sci. Instrum. **85**(4), 045108 (2014).

[40] X. Ao, J. de Boor, and V. Schmidt, "Radiation-corrected Harman method for characterization of thermoelectric materials," Adv. Energy Mater. **1**(6), 1007–1011 (2011).

[41] M.-S. Kang, I.-J. Roh, Y. G. Lee, S.-H. Baek, S. K. Kim, B.-K. Ju, D.-B. Hyun, J.-S. Kim, and B. Kwon, "Correction of the electrical and thermal extrinsic effects in thermoelectric measurements by the Harman method," Sci. Rep. **6**(1), 26507 (2016).

[42] I.-J. Roh, Y. G. Lee, M.-S. Kang, J.-U. Lee, S.-H. Baek, S. K. Kim, B.-K. Ju, D.-B. Hyun, J.-S. Kim, and B. Kwon, "Harman measurements for thermoelectric materials and modules under non-adiabatic conditions," Sci. Rep. **6**(1), 39131 (2016).

[43] A. De Marchi, V. Giaretto, S. Caron, and A. Tona, "A novel zT meter based on the porcupine method and a survey on the size of the snout correction needed for various thermoelectric devices," J. Electron. Mater. **42**(7), 2067–2072 (2013).

[44] W. E. Boyce and R. C. DiPrima, "Separation of variables," in *Elementary Differential Equations and Boundary Value Problems*, 7th ed. (Wiley, New York, 2001), pp. 605, 573–588.

[45] A. Peirce, "math257_316," Mathematics 257/316:Partial Differential Equations.

[46] Ansys Fluent | Fluid Simulation Software," 2020.

[47] P. Zhou, "Finite difference method," in *Numerical Analysis of Electromagnetic Fields*, edited by P. Zhou (Springer, Berlin, Heidelberg, 1993), pp. 63–94.

09 December 2024 11:36:47